

Chapter V

STEADY STATE LIQUID CRYSTAL THERMOGRAPHY AND HEAT TRANSFER MEASUREMENTS ON SURFACES WITH ARBITRARILY SPECIFIED BOUNDARIES

TEST CASE : FLAT ENDWALL SURFACE OF A HIGH RE NUMBER 90 ° TURNING DUCT

Cengiz Camci

THE PENNSYLVANIA STATE UNIVERSITY
Department of Aerospace Engineering

	Summary
	List of Symbols
V . 1	Introduction
V . 2	Determination of the Non-Uniform Surface Heat Flux
	Analytical Model
	Numerical Computation of Local Heat Generation
V . 3	Experimental Method and Apparatus
	Facility and Test Section
	Composite Heat Transfer Surface
	Liquid Crystal Image Processing Technique
V . 4	Experimental Results and Discussion
	Test Conditions and Data Analysis
	Application to Endwall Heat Transfer Problem
	Further Application to Film Cooled Heat Transfer Surfaces

V . 5	Experimental Uncertainty
V . 6	Conclusions
	References

Summary

The present study focuses on the accurate determination of local heat flux distributions encountered in aero propulsion convective heat transfer studies with an uncertainty level less than 4% on the heat transfer coefficient. Special emphasis is placed on a heat transfer surface with arbitrarily defined external boundaries. Flat endwall surface of a high Reynolds number 90° turning duct is used as a test case in the development of the specific liquid crystal thermography method. Heat transfer surfaces constructed for use in steady state techniques typically use thin foil type heating elements to generate a constant heat flux surface. Many of the previous studies have relied on rectangular foil shapes that generate a uniform surface heat flux distribution. Other studies that deal with geometrically complex heating elements have omitted the nonuniform heat flux regions or applied correctional techniques which are approximate. The current study combines electric field theory and a finite element method based on variational principles to directly solve for an arbitrarily specified surface heat flux distribution. Local electric energy generation per unit volume of the surface heater element in the form of local Joule heating is calculated using a differential method. The technique is shown to be applicable to many convective heat transfer configurations common in aero propulsion devices. These configurations often have arbitrarily specified external and internal geometrical boundaries such as turbine passage endwall platforms, surfaces disturbed by the existence of film cooling holes, blade tip sections, etc. A complete steady state heat transfer technique that makes use of the present local heat flux determination method is provided. Determination of the surface temperature field using liquid crystal thermography and corrections for radiative and conductive losses from the heat transfer surface is presented for the endwall surface of a 90° turning duct. The flow is fully turbulent in this square cross section duct. The solution of the surface heat flux distribution is also demonstrated for a rectangular surface that contains an array of discrete film cooling holes. The current liquid crystal method can easily be extended to any surface heater geometry that has arbitrary external or internal boundaries.

List of Symbols

CCD	=	charged coupled device for hue determination
d	=	film cooling hole diameter; (mm)
D	=	duct width; (cm)
E	=	electric field; (V/m)
h	=	heat transfer coefficient, $h=q/(T_w-T_{\infty})$; (W/m ² °K)
HSI	=	hue,saturation,intensity
J	=	current density; (A/m ²)
k	=	thermal conductivity; (W/m°K)
q	=	heat flux; (W/m ²)
R	=	total resistance; (Ω)
RGB	=	red, green, blue
rms	=	root mean square
R35C1W	=	liquid crystal starting to respond at about 35°C with an approximate color bandwidth of 1°C
R _r	=	radius ratio, $(R_i+R_o)/2D$
Re	=	Reynolds number, UD/ν
T	=	mean temperature; (°C)
U	=	mean velocity; (m/s)
V	=	electric potential; (V)
X,Y,Z	=	local coordinate system; (cm)
δ	=	Inconel thickness; (mm)
ρ	=	resistivity; (Ω·m), density; (kg/m ³)
σ	=	electrical conductivity = $1/\rho$; (Ω·m) ⁻¹
ν	=	viscosity; (m ² /s)

Subscripts

cond	=	conductive
conv	=	convective
gen	=	generated
rad	=	radiative
w	=	wall quantity
o∞	=	free stream total quantity

V . 1 Introduction

The desire to extend the cycle efficiency or to improve specific power of gas turbine engines has produced a large collection of component specific convective heat transfer research areas. Most of the emphasis in heat transfer research of gas turbine engines is directed towards the first stage guide vanes and rotor blade passages that are exposed to the hot free stream gases that originate from the combustor. In addition to the external blade passages, the internal cooling schemes of these turbine blades have also received much attention. The geometrical and environmental complexity of the turbine passage configurations requires detailed, high resolution heat transfer studies.

Convective heat transfer studies can be divided into two major experimental groups, steady state and transient. Transient experiments usually rely on a means of impulsively initiating the flow past the test surface and the assumption of a one dimensional conduction heat transfer process through the test surface. Steady state techniques rely on the construction of a heat transfer surface and are typically restricted to geometrically simple test surfaces such as flat plates and two dimensional curved surfaces. A prior knowledge of the electrically generated local heat flux on the heat transfer surface is also required. Both techniques have been widely used with considerable success. MacMullin et al. (1989) used a simple constant heat flux surface having a perfect rectangular shape in a convective heat transfer study performed on a flat plate. The steady state experiments of Boyle and Russell (1989), Hippensteele, Russell and Torres (1985), and Blair et al. (1974,1989,1991) all employed steady state techniques to investigate the convective heat transfer process in turbine blade passages. Simonich and Moffat (1984) and Wang and Simon (1987) used the steady state heat transfer technique to study the effects of concave curvature on turbulent boundary layers and convex curvature on transitional boundary layers, respectively. The heat transfer surfaces in each of these experiments were geometrically simple and the resultant surface heat flux was uniform. Film cooling studies by Eriksen and Goldstein (1974), Mick and Mayle (1988), Ou et al. (1992 a,b), and Mehendale and Han (1992) were also performed using the steady state heat transfer technique. Film cooling studies represent a geometrical configuration that introduce a complication to steady state experiments. Significant variations in both the film cooling effectiveness and the local heat transfer coefficient may occur within the near cooling hole regions. To experimentally resolve the heat transfer characteristics in this area, the generated local surface heat flux levels must be accurately determined. Due to the geometrical complexity of the heat flux surface boundaries, the current density field and the electric field will distort to a condition that a uniform heat flux assumption becomes weak. Several studies including Mick and Mayle (1988) and Mehendale and Han (1992) have used correctional techniques to determine the surface heat flux variations near the film cooling holes. Discrete point thermocouples were used to map the surface temperature distributions of the local regions where the heat flux distributions significantly deviated from a constant value.

An alternative method to the correctional technique is a direct calculation of the generated surface heat flux at each point of the heater surface using electrostatic theory. In addition to film cooling studies, the direct calculation approach presented in this study can be adapted to many other complex, two dimensional heater surface geometries that have arbitrarily specified external and internal boundaries. The endwall surface of a turbine passage, the tip surface of a rotor blade, local surfaces of an internal cooling arrangement in a turbine blade are a few examples of arbitrarily specified component surfaces.

The objective of the current study is to present a complete procedure for determining local convective heat transfer coefficients in steady state experiments when the heater shape is not rectangular. The procedure can also take into account arbitrarily specified cooling holes and slots on the heat transfer surface. Local generation of Joule heating through internal electrical

heat generation can be accurately determined by solving the partial differential equation governing the potential distribution on the heater element even with arbitrarily specified internal and external boundaries. The complete method is demonstrated for the endwall surface of a 90° turning duct in which a fully turbulent flow exists at the inlet section. The influence of film cooling holes on the local Joule heating distribution of a heat transfer surface is also demonstrated. The method uses second order accurate quadrilateral finite elements to discretize the heat flux surface and a variational principle known as Euler's theorem to determine the heat flux distribution accurately. High resolution surface temperature distributions were resolved using chiral nematic liquid crystals, a high sensitivity CCD sensor, and an HSI domain image processor. Radiative and conductive losses from the composite heat transfer surface were also taken into account. Deviations from the one-dimensional conduction loss model have been incorporated into the uncertainty analysis.

V . 2 Determination of the Non-uniform Surface Heat Flux

V.2.2 Analytical Model : Determination of the steady heat flux field on an arbitrarily specified heat transfer surface requires the solution of an electrostatic boundary value problem. For a two dimensional, linear, isotropic, homogeneous conducting medium with zero free charge, the electric potential must satisfy,

(5.1)

For thin foil heaters, such as Inconel foil ($\delta=0.025$ mm), the thickness of the foil relative to the surface area is such that negligible current conducts in the direction normal to the surface plane. Therefore, the current and potential fields are two dimensional. The electrical boundary conditions for the heater surface are a uniform potential at the bus bar and Inconel foil junctions and zero current flow normal to the two unbounded streamwise edges, Figure 1. An electric field vector \mathbf{E} can be

defined as the gradient of the scalar potential field, $V(x,y)$.

(5.2)

The negative sign is introduced to account for the conventional coordinate system used. Once the electric potential and field are resolved, the current density field, \mathbf{J} , can be determined by a scalar multiplication of the electric field and the electrical conductivity of the medium, σ .

(5.3)

The conductivity of a medium is a material property equivalent to the inverse of the resistivity ρ . The relationship between the conductivity and the electrical resistance of a medium of simple geometry is illustrated in Figure 2. The power density within a medium under steady current conditions is a point function determined from the dot product of the electric field and current density, $\mathbf{E} \cdot \mathbf{J}$ (W/m^3). Therefore, the electric power converted into heat per unit surface area is

$$(5.4)$$

where, δ is the thickness of the conducting medium. The solution of the electrostatic boundary value problem is analogous to a conduction heat transfer solution in which the temperature field is solved for in a given domain rather than the electric potential. In the electrostatic solution, the current density field is analogous to the thermal conduction heat flux field. A prescribed temperature boundary condition of the thermal conduction problem is analogous to a specified electric potential condition such as the bus bar locations shown in Figure 1. A zero electric current flux condition normal to a boundary or edge corresponds to an adiabatic condition in the thermal problem. This analogy conveniently lends itself to the application of any existing solution technique of a two dimensional conduction heat transfer boundary value problem to the electrostatic domain.

V.2.2 Numerical Computation of the Local Heat Generation : In the current study, the electric potential and current density distributions of the endwall heat transfer surface were determined using the solution method described in the previous paragraph. The heat transfer surface was discretized with eight noded, isoparametric, quadrilateral finite elements. The computational domain contained a total of 402 nodes and 104 elements. A technique based on variational principles was used to solve for the potential and current density distributions. The essence of the technique is the minimization of an integral relation, equation 5.5, for each element in the domain.

$$(5.5)$$

The minimization technique is analogous to satisfying the Laplace equation (equation 5.1) over the entire domain. The procedure results in a set of linear algebraic equations that are then solved simultaneously to provide the electric potential field with the prescribed boundary conditions. Further details of the numerical technique is given in Zienkiewicz (1971) and Camci (1989).

V . 3 Experimental Method and Apparatus

V.3.1 Facility and Test Section : The surface under consideration was the endwall of a square cross section, 90° turning duct. The test section was constructed of 1.27 cm thick flat endwalls and 0.476 cm thick curved side walls of clear acrylic. The test section was located on the downstream side of an open loop wind tunnel. The facility consisted of an axial blower, diffuser with multiple screens, plenum chamber, high area ratio nozzle, circular to rectangular transition nozzle, a section of constant cross section duct, and the test section. The constant cross section duct that preceded the test section housed several additional screens. Further details of the tunnel are provided in Wiedner and Camci (1992). An illustration of the endwall test section geometry and coordinate system is shown in Figure 1. The 90° bend has a radius ratio, R_r , of 2.3 and cross section width of 20.3 cm. The exit of the test section was directed towards the floor with the exit plane at a height of 85 cm from the floor. This orientation provided an unobstructed side view of the endwall heat transfer surface. The heat transfer measurements were performed at an inlet free stream velocity of 28.3 m/s. The free stream air was at ambient temperature.

V.3.2 Composite Heat Transfer Surface : A detailed view of the surface composite is shown in Figure 3. The surface consists of several layers that include double sided tape, Inconel 600 foil, black paint, and chiral nematic encapsulated (R35C1W) liquid crystals. A low resistivity steel foil, Inconel 600, was used as the heater material. The material has a low temperature coefficient of resistivity ($0.112 \times 10^{-3} \text{ }^\circ\text{C}^{-1}$) that restrains a change in the resistance of the foil within the experimental temperature range (less than 0.23%). Inconel foil is made up of 75% Ni, 15% Cr and 10% Fe. The heat transfer surface begins 50.8 cm upstream of the 0° position and ends 2 cm past the 90° position as shown in Figure 1. At the upstream end of the test surface, the foil exited the test section at a flange interface. The downstream end passed through a transverse slot cut in the endwall acrylic. To minimize conduction to the endwall surface at the foil entry and exit planes, the foil was fitted between two 0.476 cm balsa sections. On the ambient side of the endwall, copper bus bars were connected to the foil by compression contact. To minimize contact resistance and prohibit oxidation, the contact faces of the copper bus bars were machined smooth, chemically cleaned in an acid bath and plated. A cascade immersion process was used to deposit a 0.5 μm dense plate tin film. To ensure an equipotential boundary condition existed at the bus bar and foil junction, large 1.27 cm square cross sectioned bus bars were used. An experimental verification indicated less than 0.1% potential variation existed across the bus bar length. A 1000 watt, variable current DC power supply was used to heat the heat transfer surface. Two K-type thin foil thermocouples were located on the foil surface for calibration of the liquid crystals. They were fastened with double sided Kapton tape (0.1 mm thick). The physical properties of the Kapton tape (resistivity, $3 \times 10^{14} \text{ } \Omega\text{cm}$ and thermal conductivity, 0.37 W/m°K) provided excellent electrical isolation and thermal contact of the thermocouple junction and leads with the heat flux surface. The surface was then covered with flat black background

paint and four equivalent layers of chiral nematic encapsulated liquid crystal (R35C1W) using an air brush technique.

V.3.3 Liquid Crystal and Image Processing Techniques : The liquid crystal image capturing and processing techniques adapted in the present study are described fully in Camci, Kim and Hippensteele (1992) and Kim (1991). In summary, an NTSC standard 24-bit color image processing system was used to convert multiplexed RGB information to HSI information on each pixel of a 512×480 image. The RGB attributes of an image were captured with a high sensitivity CCD sensor that acquired complete images at a rate of 30 Hz. The system uses three 8-bit video A/D converters; therefore, each of the three RGB or HSI attributes of an image vary between 0 and 255. A linear hue versus temperature relation was determined through calibration for each camera and illumination configuration used in the study. All surface temperature information was obtained from the hue attribute of an image. Previous work with the image processing system has shown that local hue values become unstable at high and low intensities Kim (1991); therefore, the intensity attribute was used as a filter.

The endwall heat transfer surface temperatures were mapped using a chiral nematic encapsulated liquid crystal with an event temperature of approximately 35°C and bandwidth of 1°C. To minimize the deviation of the viewing angle from normal, three camera positions were used to capture the complete endwall surface. In addition, two images were acquired with a change in the zoom position of the camera lens. The illumination sources for each of the views were two 500 W, 3200°K incandescent lamps. For all experiments, the camera configuration, and illumination setup were identical between calibration runs and heat transfer tests. The calibration of the crystals was performed in a slow transient fashion using the heater surface and the variable power supply to cycle the surface through the liquid crystal event range. Each cycle of the slow transient experiment took about 20 seconds between the appearance of the first red and first blue colors. Two thin foil thermocouples were located on the endwall surface in view of the video camera. The thermocouple output voltage was converted to temperature and also displayed in the calibration images. The response time of the thermocouples was approximately 3-5 msec. The thin film thermocouple and associated amplifier circuitry were calibrated against an approximately zero bias mercury thermometer prior to the liquid crystal calibration. Before each calibration transient, the pixel coordinates of the thermocouple junction were identified in the image. Hue information and the corresponding surface temperature could then be extracted at successive images at the precise pixel (coordinate) location of the thermocouple junction. The calibration results of one camera view of the heat transfer surface for three individual heating cycles is shown in Figure 4. In addition, the effects of altering the zoom position of the camera lens are also shown. The change in the zoom position of the camera resulted in a pixel resolution twice that of the other positions. Each data symbol in the figure represent an average of approximately thirty frames of video image acquired in the slow transient process. The frame/hue averaging technique was found to reduce the noise level in each image that is common to commercially available high sensitivity CCD sensors and magnetic tape storage mediums.

The surface temperatures that were extracted in each of the heat transfer tests were restricted to a hue range of 40 to 160. A linear regression analysis was performed on the calibration data in this range and the results including a 95% confidence interval have been superimposed on the raw calibration data, Figure 4.

The same frame averaging technique was used to process the images from each heat transfer test. The hue, saturation and intensity attributes of consecutive frames of steady state endwall color display were temporally averaged and stored to compose a final mean image. The mean images were then scanned pixel by pixel in search of HSI values that met a predetermined filter criteria. Each of the mean images analyzed in this study were band pass filtered in the hue domain at 40-160. The pixels with intensity attributes less than 25 and greater than 200 were also eliminated to avoid possible unstable hue conversion. All of the hue and intensity values described were in 8-bit scale with a maximum value of 255.

V . 4 Experimental Results and Discussion

V.4.1 *Test Conditions and Data Analysis* : All heat transfer tests were conducted at a Reynolds number of approximately 360,000 based on the inlet centerline velocity, duct width and ambient free stream conditions. The results of a single sensor hotwire profile measured at a distance of 5 cm upstream of the heat transfer surface and at $Y/D = 2.30$ are shown in Figure 5. The mean velocity profile indicates a boundary layer thickness of 2.54 cm ($Z/D=0.125$), and uniform free stream conditions. The streamwise velocity fluctuations had a rms level of 0.7% of the mean velocity in the free stream and a peak of 6.8% of the free stream mean velocity within the endwall boundary layer. The objective of this work was to provide a detailed description of the technique employed to obtain high resolution heat transfer information in geometrically complex configurations; therefore, with the exception of the Reynolds number and the description of fully turbulent inlet conditions, the aerodynamic qualities of the duct flow have been excluded. The details of the duct aerodynamics are included in Wiedner (1993). The heat transfer results presented were obtained from 23 steady state experiments conducted at different input power levels to the electric heater. Steady state conditions required approximately two hours to achieve. The thermal conditions on the convective heat transfer side of the endwall, ambient side of the endwall and the tunnel free stream were used to indicate steady state conditions. The primary focus of the heat transfer tests was to quantitatively resolve the convective heat transfer coefficient on the endwall surface. The heat transfer coefficient was determined according to,

To account for conduction losses through the acrylic endwall, temperature measurements were recorded at multiple locations on the ambient side surface. The measurement locations were clustered near the corresponding area of the liquid crystal event region that existed on the convective side of the surface. The temperature measurements on the ambient side of the endwall surface were recorded with an infrared thermometer. The same mercury thermometer used to calibrate the thin foil thermocouples on the heat transfer side of the test section was used to calibrate the infrared thermometer. To calibrate the infrared thermometer, a known surface temperature was first recorded. The calibration constant of the infrared thermometer (emissivity of the surface) was then adjusted until the infrared thermometer indicated the true temperature of the surface. A uniform surface emissivity is required for a local surface calibration to be valid over the entire surface. This was obtained by air brush spraying the acrylic surface with flat black paint. The uniform emissivity criteria was then experimentally verified with the thermometer. During a typical steady state, heat transfer experiment, the ambient side of the endwall exhibited a temperature variation of approximately ± 0.5 °C and a distribution similar to the temperature distribution depicted by the liquid crystals on the inner, forced convection side of the endwall. The conduction losses were calculated locally at each pixel coordinate in which hue/temperature information was available. The corresponding ambient side temperature of the endwall was determined from a high density grid of the infrared thermometer measurements. A two dimensional interpolation scheme was used to calculate the temperature grid. The conduction losses through the endwall surface were estimated including the effects of lateral conduction on the back surface (ambient side) of the endwall. The significance of lateral conduction on the total conduction loss was documented in several areas on the endwall surface, Figure 6. The maximum local lateral conduction component found on the back surface had a magnitude of 19.2% of the respective normal component. This resulted in an increased conduction heat flux loss of less than 0.25% of the local generated heat flux. The conduction losses typically accounted for approximately 5-8% of the generated heat flux. Local radiation losses from the heat transfer surface were approximated using an enclosure model and considering each surface as black. The unheated duct walls were assumed to be in thermal equilibrium with the free stream. The heat flux lost to radiation from the heater surface accounted for approximately 8-10% of the generated heat flux. The free stream temperature upstream of the test section was measured using a fine wire K-type thermocouple probe. The thermocouple probe was calibrated in a static environment with the same mercury thermometer as each of the other temperature indicators. A recovery factor of unity was assumed due to the low speed character of the inlet flow. When the endwall surface images were obtained, a short duration 'pulse' of the illumination lamps was used to minimize the thermal radiation heat flux

originating from the lamps. A test was performed in which the hue attribute of several discrete pixels in a series of images from a steady state test were extracted. Over the duration of the illumination period, the hue value at each pixel evaluated was constant. This test showed that the radiation heat flux contribution to the surface temperature measurement was minimal.

The temperature information from an image was mapped from pixel to duct coordinates using several previously marked reference points on the test section surface. The white reference points allowed easy identification by the image processor due to the high intensity attribute. For a given heat transfer test, the coordinates of an endwall region that contained the hue attributes between 40 and 160 could be extracted. These pixels provided accurate wall temperature measurements at high resolution after the hue to temperature conversion, Figure 4. To match the spatial resolution of the surface temperature distribution, a high density grid of the generated surface heat flux was produced using the same interpolation scheme as used for the ambient side temperature distribution. After locally correcting the surface heat flux distribution for conduction and radiation losses, the convective heat transfer coefficient was calculated based on the wall to free stream temperature difference, equation 5.6.

V.4.2 Application to Endwall Heat Transfer Problem : Results of the numerical procedure described for the solution of the electrostatic boundary value problem are shown in Figures 7-10. The calculations were performed for a unit drop in potential across the bus bars. A 1 VDC equipotential line at the leading edge of the foil, $X/D=0.0$, and a 0 VDC equipotential line at the trailing edge of the foil, $Y/D=-0.1$, were used as the prescribed potential boundary conditions. The numerically predicted potential field for the endwall heat flux surface is shown in Figure 7 and an experimentally determined potential field is shown in Figure 8. Several predicted equipotential contours are included with the experimental measurements. The comparison indicates that the numerical results sufficiently predict the potential distribution on the endwall. The initiation of the endwall/duct curvature occurs at a distance of $X/D=2.5$; however, the elliptic nature of the electrostatic field causes an increased potential drop along the lower surface relative to the upper surface before this point. This effect is most evident in the bend of the 0.60 and 0.65 contour levels. The elliptic effect is also seen in current density field, Figure 9. At $X/D=2.5$ (0°), the current density vectors show a gradient in magnitude from the lower to the upper edge. Also, as the 0° plane is approached, the direction of the current density field is seen to shift downwards from horizontal. Physically, the uniform current density field which enters the foil at the leading edge bus bar, $X/D=0.0$, is searching for the path of least resistance. According to the description illustrated in Figure 2, this

occurs for a condition of shortest path and largest cross sectional area between bus bars. The transverse gradient in the current density field through the curve, as well as, upstream of the curve represents the current density field's interpretation of this condition. The combination of both the potential field and the current density field, as modelled by equation 5.4, is shown as the distribution of the generated surface heat flux, Figure 10. A strong variation of local heat flux exists throughout the curved portion of the endwall, whereas a weaker variation is evident upstream. For example, a 0.4% variation in the surface heat flux exists along the endwall centerline between the foil leading edge ($X/D=0.0$) and $X/D = 0.5$.

The results of 23 steady state heat transfer experiments are shown as a complete map of the endwall convective heat transfer coefficient distribution in Figures 11(a) and (b). The map was obtained from a series of experiments performed at different surface heat flux levels (potential drops across the bus bars). For each experiment, the liquid crystal color play region was located in a different region of the endwall surface. The 23 experiments required to achieve a high resolution heat transfer coefficient map was due in part to the large test section (multiple camera views) and narrow band width of the liquid crystals (high resolution).

V.4.3 Further Application to Film Cooled Heat Transfer Surfaces : To demonstrate the capability of the present method in another common area of turbine heat transfer, a square heat flux surface with an array of film cooling holes has been solved. The geometry of the heat flux surface and the finite element discretization are shown in Figure 12. The computational domain contained 144 eight noded, isoparametric, quadrilateral elements and 490 nodes. The surface coordinates have been nondimensionalized by the cooling hole diameter. The film cooling hole pattern is a 1×3 array of 3 mm diameter holes that are inclined 30° to the foil surface and spaced 3 diameters apart. The conducting medium is Inconel foil ($\delta=0.025$ mm) and a 1 mVDC potential drop was prescribed across bus bars located on the left and right edges. A zero current flux condition normal to the top and bottom surfaces was also prescribed. The generated surface heat flux distribution is shown in Figure 13. For a simple square heat flux surface without film cooling holes, a uniform heat flux of 190 W/m^2 would exist. Introducing the holes in the surface increases the total resistance of the foil, thus for the same 1 mVDC potential drop across the bus bars, the heat flux far from the holes decreases to approximately 175 W/m^2 . More importantly, the local surface heat flux levels in the near field of the cooling holes indicate severe variations. A maximum generated heat flux of 656 W/m^2 exists on each of the upper and lower edges of the cooling holes. The minimum heat flux regions occur near the stagnation regions of the current field located at the left most and right most edges of the holes.

V . 5 Experimental Uncertainty

The experimental uncertainty in the convective heat transfer coefficient was estimated according to the procedures detailed by Kline and McClintock (1953) and Abernethy et al. (1985). The following list summarizes the initial sources of error and the propagation of the source precision and bias errors to the final uncertainty in the heat transfer coefficient. The uncertainty level quoted is analogous to 95% coverage. The exact nature of the finite element numerical procedure and minimization of the conductive and radiative heat flux losses results in a low measurement uncertainty of the generated heat flux and consequently a low uncertainty level for the convective heat transfer coefficient.

	Precision Index	Bias Error	Uncertainty
q_{gen}	1.0%	0.3%	1.0%
q_{cond}	5.5%	5.9%	8.1%
q_{rad}	1.6%	1.9%	2.5%
T_{∞}	1.0%	0.8%	1.3%
$T_w - T_{\infty}$	2.7%	2.6%	3.4%
h	2.8%	2.7%	3.8%

The heat loss to conduction through the endwall was considered one-dimensional in the error and uncertainty values provided. An analysis that considered multi-dimensional conductive heat loss indicated a maximum variation in the heat transfer coefficient to be less than 0.25% of the reported value. The variation in resistivity of the heater material due to temperature changes was found to be less than 0.23% within the experimental temperature range. This effect has been included in the uncertainty levels provided. A complete discussion of the error analysis is given in Wiedner (1993).

V . 6 Conclusions

A numerical solution technique based on electric field theory was used to directly solve a nonuniform surface heat flux distribution for two different geometries common in aero propulsion heat transfer studies. The complete numerical and experimental technique was demonstrated for the endwall surface of a strongly curved 90° duct flow. The solution of the nonuniform surface heat flux distribution was also shown for a heat transfer surface that contained a 1×3 array of film cooling holes. Significant variations in the local generated heat flux were evident in both configurations. Liquid crystal thermography and correctional techniques for conductive and radiative heat flux losses were combined with the numerical solution of the generated surface heat flux to provide convective heat transfer coefficient levels on the endwall surface of the 90° turbulent duct flow. The hue, saturation, and intensity attributes of 30 consecutive frames were temporally averaged for the first time to reduce the uncertainties in the hue/temperature conversion. This process successfully eliminated some of the inherent noise that exists in high sensitivity imaging sensors. The method resulted in an estimated uncertainty of 3.8% for the convective heat transfer coefficient. The present method is suitable for extracting high resolution heat transfer information from many complex, two dimensional configurations that have nonuniform surface heat flux distributions. The current finite element based method can take the local variation of heater foil thickness into account. Although the resistivity of the current heater element, Inconel 600, did not vary within the experimental surface temperature range, the specific approach can successfully model local variations in heater resistivity due to temperature dependency.

References

- Abernethy, R. B., Benedict, R. P., and Dowdell, R. B., 1985, "ASME Measurement Uncertainty," *ASME Journal of Fluids Engineering*, Vol.107, pp. 161-164.
- Arts, T. A., Lambert de Rouvroit, M., Rau, G., and Acton, P., 1992, "Aerothermal Investigation of the Flow Developing in a 180 Degree Turn Channel," *Proceedings of the 1992 Inter-national Symposium on Heat Transfer In Turbomachinery*, Marathon, Greece.

Blair, M. F., 1974, "An Experimental Study of Heat Transfer and Film Cooling on Large Scale Turbine Endwalls," *ASME Journal of Heat Transfer*, Vol.96, pp. 524-529.

Blair, M. F., Dring, R. P., and Joslyn, H. D., 1989, "The Effects of Turbulence and Stator/Rotor Interactions on Turbine Heat Transfer: Part:I Design Operating Conditions," *ASME Journal of Turbomachinery*, Vol.111, pp. 87-95.

Blair, M. F., Wagner, J. H., and Steuber, G. D., 1991, "New Applications of Liquid-Crystal Thermography in Rotating Turbomachinery Heat Transfer Research," ASME paper 91-GT-354.

Blair, M. F., 1983, "Influence of Free Stream Turbulence on Turbulent Boundary Layer Heat Transfer and Mean Profile Development, Part-I Experimental Data," *ASME Journal of Heat Transfer*, Vol.105, No.1, pp. 33-40.

Boyle, R. J. and Russell, L. M., 1989, "Experimental Determination of Stator Endwall Heat Transfer," *ASME Journal of Turbomachinery*, Vol.112, pp. 547-558.

Camci, C., 1989, "An Experimental and Numerical Investigation of Near Cooling Hole Heat Fluxes on a Film Cooled Turbine Blade," *ASME Journal of Turbomachinery*, Vol.111, pp. 63-70.

Camci, C., Kim, K., and Hippensteele, S. A., 1992, "A New Hue Capturing Technique for the Quantitative Interpretation of Liquid Crystal Images Used in Convective Heat Transfer Studies," *ASME Journal of Turbomachinery*, Vol.114, pp. 765-775.

Eriksen, V. L. and Goldstein, R. J., 1974, "Heat Transfer and Film Cooling Following Injection Through Inclined Circular Tubes," *ASME Journal of Heat Transfer*, Vol. 96, pp. 239-245.

Hippensteele, S. A., Russell, L. M., and Torres, F. J., 1985, "Local Heat Transfer Measurements on a Large Scale Model Turbine Blade Airfoil Using a Composite of Heater Element and Liquid-Crystals," *ASME Journal of Gas Turbines and Power*, Vol. 107, pp. 953-960.

Kim, K., 1991, "A New Hue Capturing Technique for the Quantitative Interpretation of Liquid Crystal Images Used in Convective Heat Transfer Studies," Ph.D. Thesis, The Pennsylvania State University, Aerospace Engineering Department.

Kline, S. J. and McClintock, F. A., 1953, "Describing Uncertainties in Single Sample Experiments," *Mechanical Engineering*, Vol.75, p. 3.

MacMullin, R., Elrod, W., and Rivir, R., 1989, "Free-Stream Turbulence From a Circular Wall Jet on a Flat Plate Heat Transfer and Boundary Layer Flow," *ASME Journal of Turbomachinery*, Vol.111, pp. 78-86.

Mehendale, A. B. and Han, J. C., 1992, "Influence of High Mainstream Turbulence on Leading Edge Film Cooling Heat Transfer," *ASME Journal of Turbomachinery*, Vol.114, pp. 707-715.

Mick, W. J. and Mayle, R. E., 1988, "Stagnation Film Cooling and Heat Transfer, Including Its Effect Within the Hole Pattern," *ASME Journal of Turbomachinery*,

Vol.110, pp. 66-72.

Ou, S., Mehendale, A. B., and Han, J. C., 1992a, "Influence of High Mainstream Turbulence on Leading Edge Film Cooling Heat Transfer: Effect of Film Hole Row Location," *ASME Journal of Turbomachinery*, Vol.114, pp. 716-723.

Ou, S. and Han, J. C., 1992b, "Influence of Mainstream Turbulence on Leading Edge Film Cooling Heat Transfer Through Two Rows of Inclined Film Slots," *ASME Journal of Turbomachinery*, Vol.114, pp. 724-733.

Simonich, J. C. and Moffat, R. J., 1984, "Liquid Crystal Visualization of Surface Heat Transfer on a Concavely Curved Turbulent Boundary Layer," *ASME Journal of Engineering for Gas Turbines and Power*, Vol.106, pp. 619-627.

Wang, T. and Simon, T. W., 1987, "Heat Transfer and Fluid Mechanics Measurements in Transitional Boundary Layers on Convex-Curved Surfaces," *ASME Journal of Turbomachinery*, Vol.109, pp. 443-450.

Wiedner, B. G., 1993, "Passage Flow Structure and Its Influence on Endwall Heat Transfer in a 90° Turning Duct," Ph.D. Thesis, The Pennsylvania State University, Aerospace Engineering Department.

Wiedner, B. and Camci, C., 1992, "A Low Speed, Transient Facility for Propulsion Heat Transfer Studies," proceedings of the International Symposium on Heat Transfer in Turbomachinery, August 24-28, Athens, Greece.

Zienkiewicz, O. C., 1971, *The Finite Element Method in Engineering Science*, McGraw-Hill, London.

Fig. 5.1 Endwall heat transfer surface geometry.

Fig. 5.2 Relationship between the resistance, conductivity and resistivity for a simple geometry conducting medium.

Fig. 5.3 Detailed cross section of the heat transfer surface composite.

Fig. 5.4 Liquid crystal calibration with temporal averaging.

Fig. 5.5 Mean and fluctuating velocity profiles 5 cm upstream of the heat transfer surface at the endwall centerline, $Y/D = 2.3$.

Fig. 5.6 Effects of lateral conduction heat loss on calculation of the convective heat transfer coefficient.

Fig. 5.7 Numerically determined electric potential distribution (V) on the endwall heat transfer surface, 1 VDC potential drop across the bus bars.

Fig. 5.8 Experimentally determined electric potential distribution (V) on the endwall heat transfer surface, 1 VDC potential drop across the bus bars, selected contour levels superimposed from the numerical results.

Fig. 5.9 Vector representation of the current density field (A/m^2) of the endwall heat transfer surface for a 1 VDC potential drop across the bus bars.

Fig. 5.10 Distribution of the generated heat flux (W/m^2) on the endwall heat transfer surface for a 1 VDC drop in potential across the bus bars.

Fig. 5.11 (a) (b) Convective heat transfer coefficient (W/m^2K) distribution on the endwall surface. Data represents the results of twenty three processed images.

Fig. 5.12 Illustration of the heat flux surface geometry and finite element computational grid for a square surface with a 1×3 array of film cooling holes inclined 30° from the surface at a spacing of $Y/d=3$.

Fig. 5.13 Distribution of the generated heat flux (W/m^2) for a square surface that contains a 1×3 array of film cooling holes inclined 30° to the surface at a spacing of $Y/d=3$. Potential drop of 1 mVDC across the bus bars.

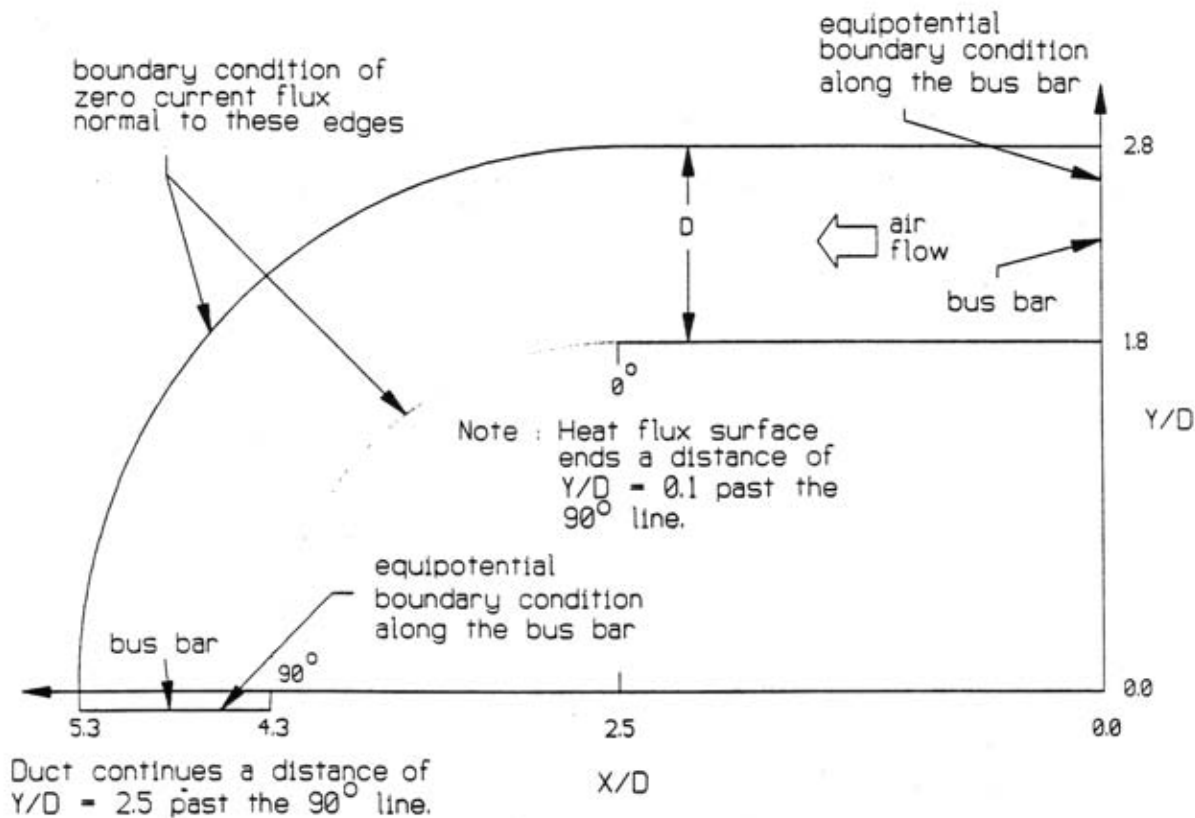


Fig. 5.1 Endwall heat transfer surface geometry.

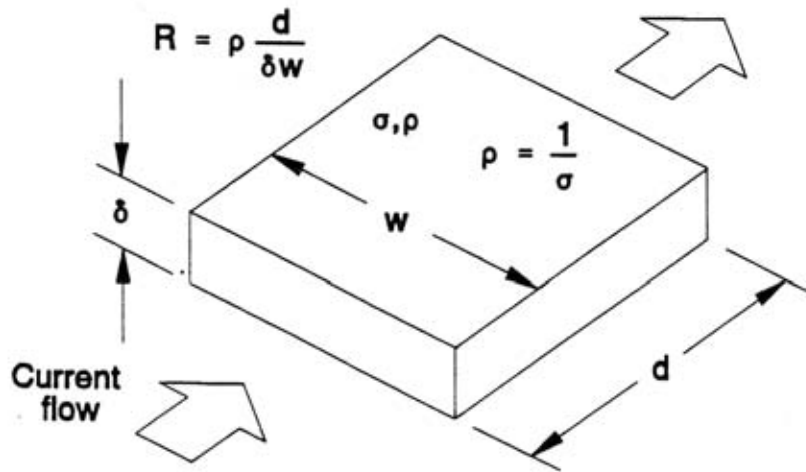


Fig. 5.2

Relationship between the resistance, conductivity and resistivity for a simple geometry conducting medium.

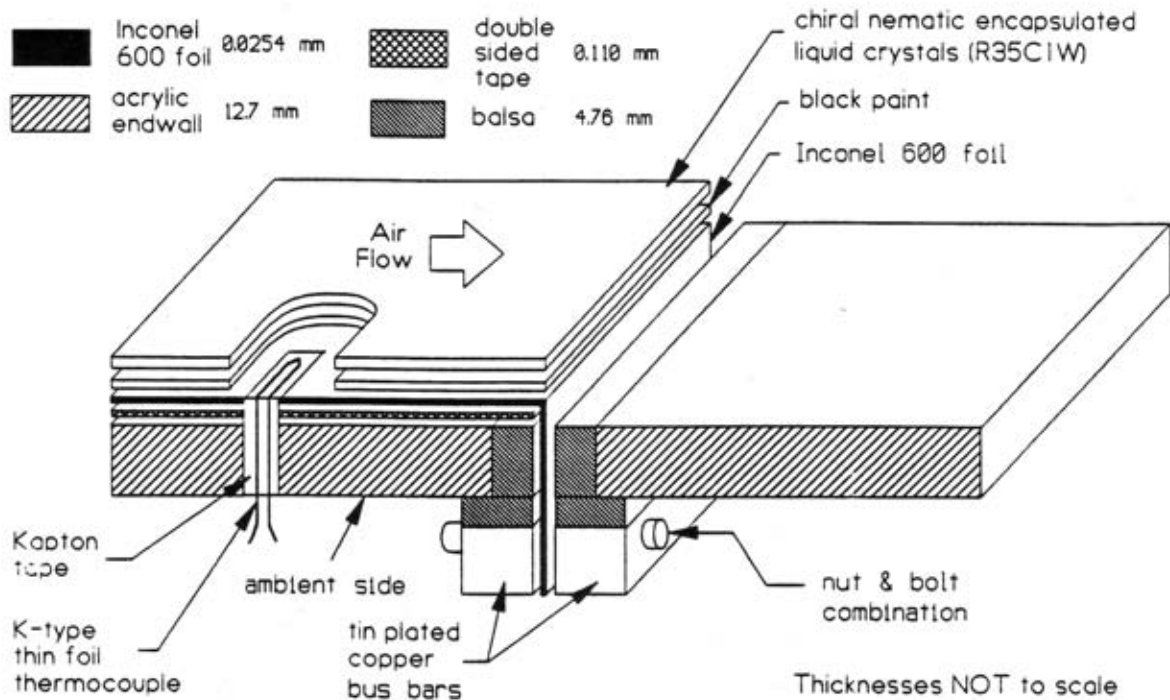


Fig. 5.3

Detailed cross section of the heat transfer surface composite.

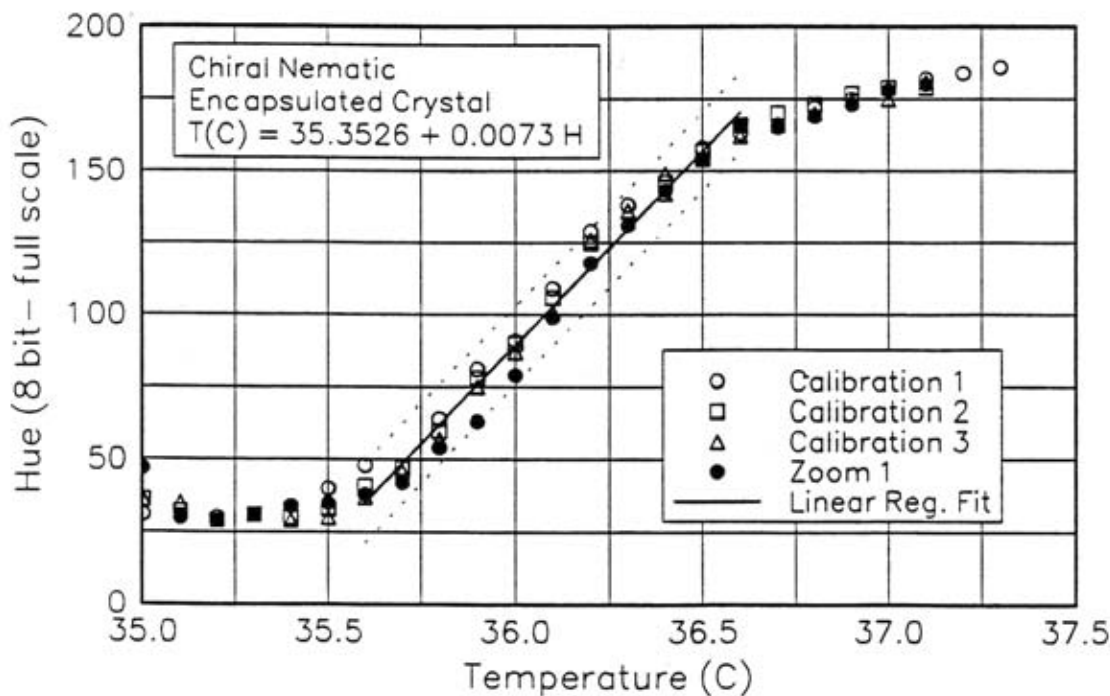


Fig. 5.4 Liquid crystal calibration with temporal averaging.

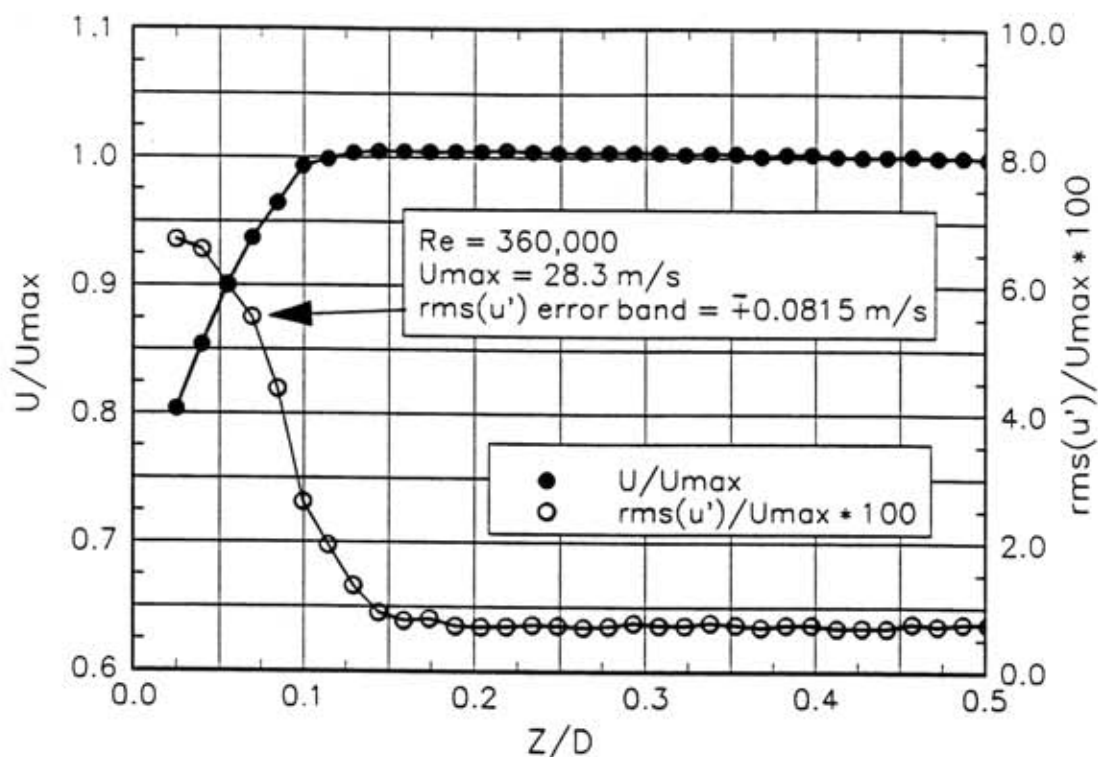


Fig. 5.5 Mean and fluctuating velocity profiles 5 cm upstream of the heat transfer surface at the endwall centerline, $Y/D = 2.3$.

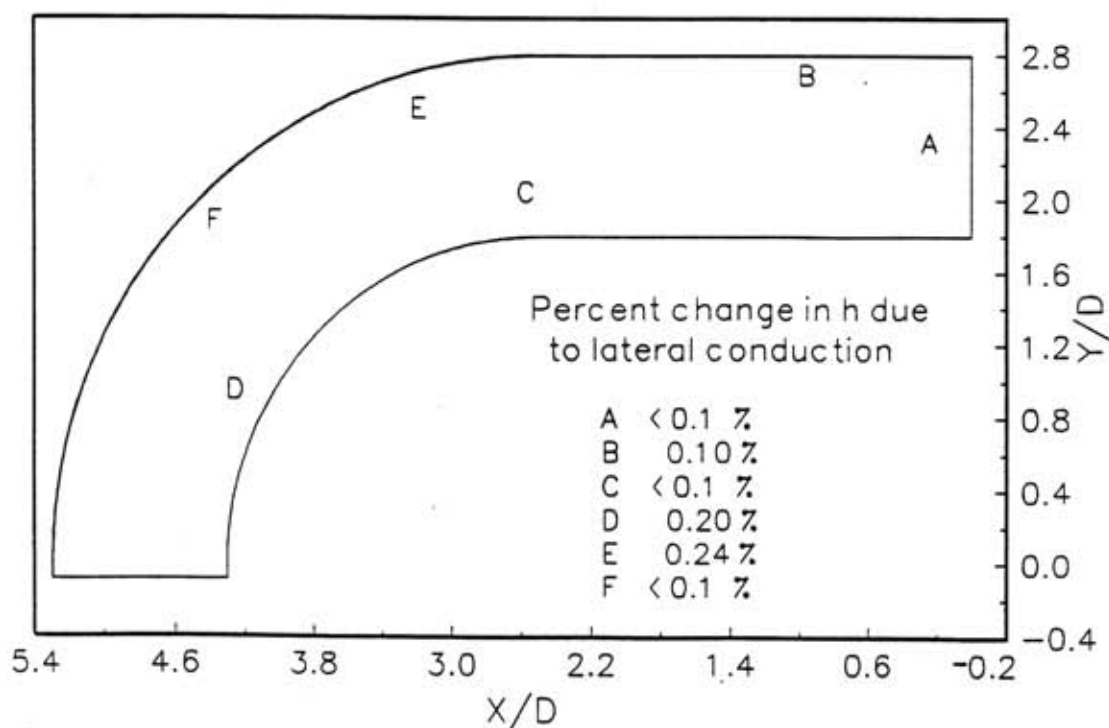


Fig. 5.6 Effects of lateral conduction heat loss on calculation of the convective heat transfer coefficient.

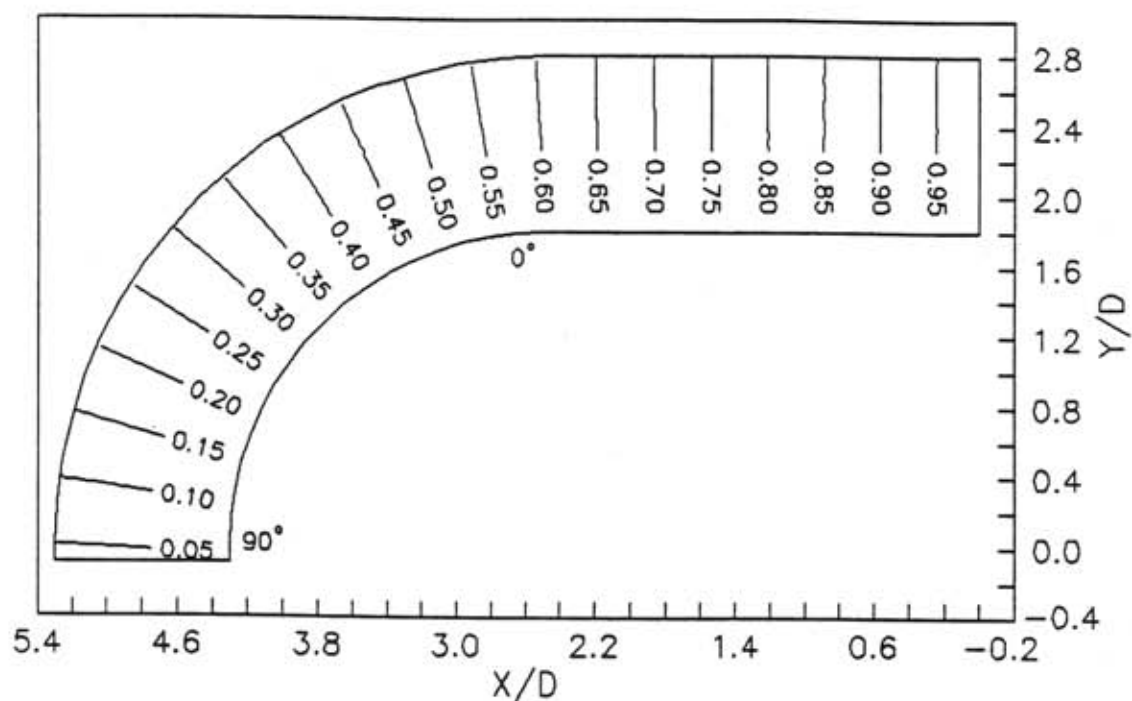


Fig. 5.7 Numerically determined electric potential distribution (V) on the endwall heat transfer surface, 1 VDC potential drop across the bus bars.

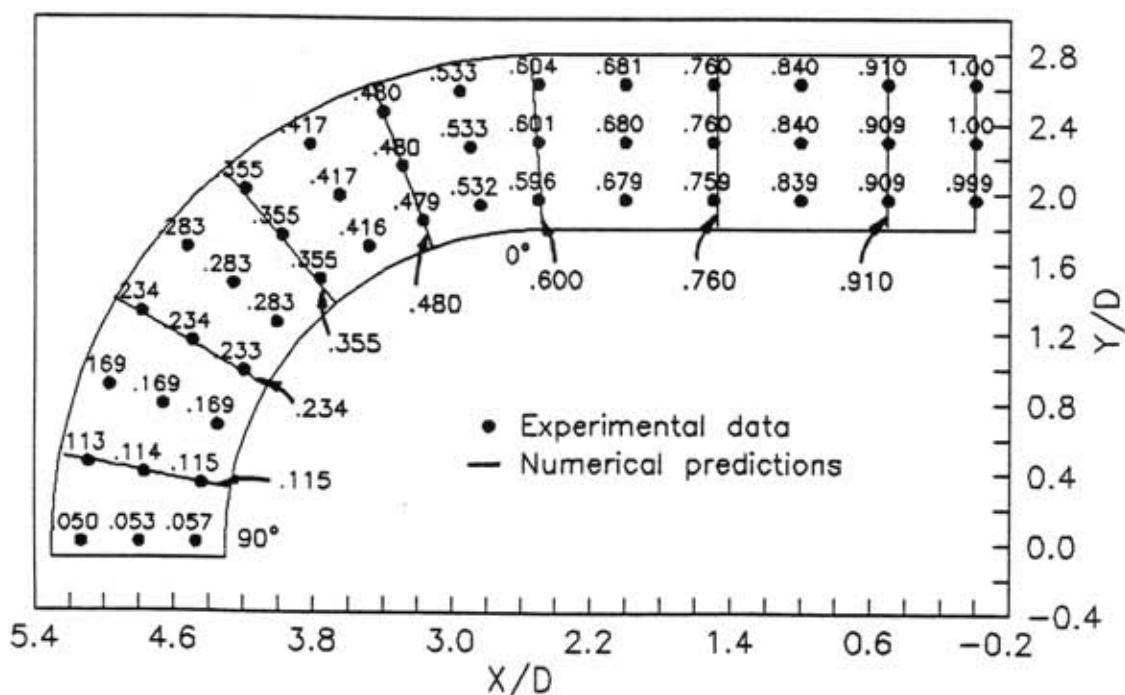


Fig. 5.8 Experimentally determined electric potential distribution (V) on the endwall heat transfer surface, 1 VDC potential drop across the bus bars, selected contour levels superimposed from the numerical results.

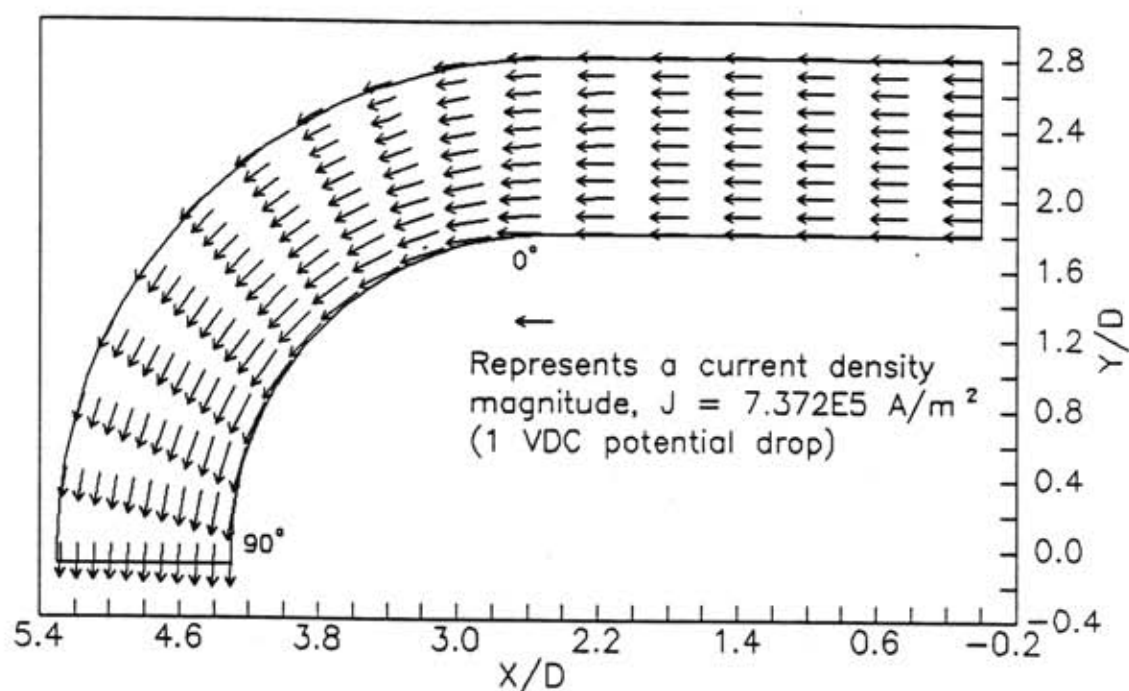


Fig. 5.9 Vector representation of the current density field (A/m^2) of the endwall heat transfer surface for a 1 VDC potential drop across the bus bars.

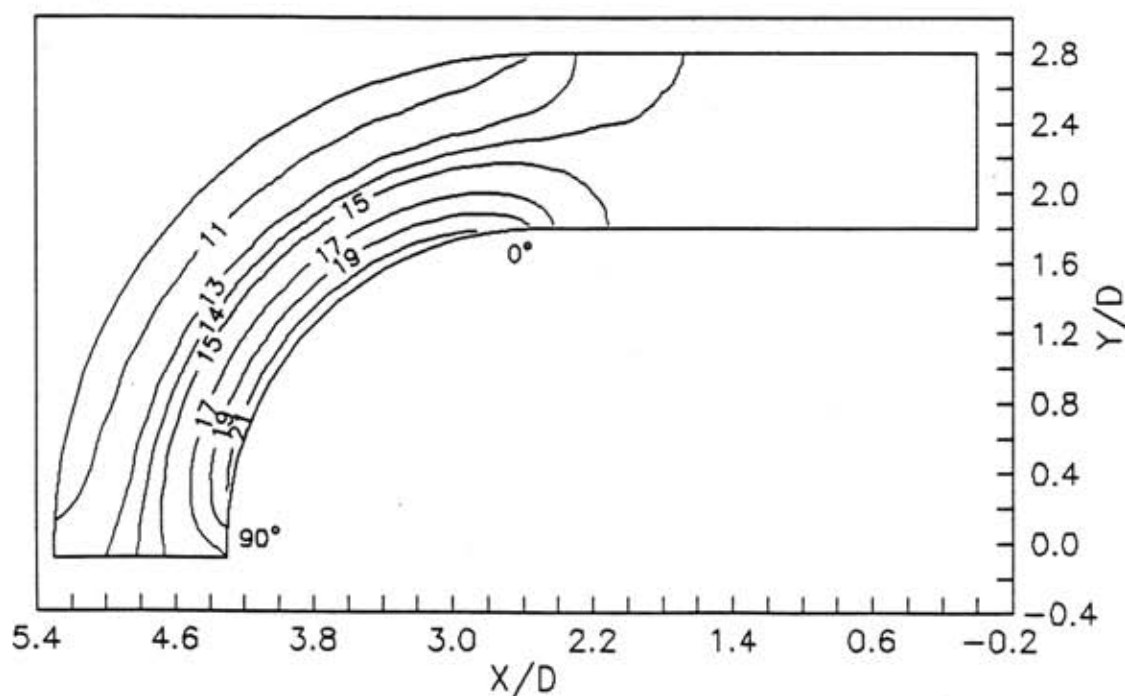


Fig. 5.10 Distribution of the generated heat flux (W/m^2) on the endwall heat transfer surface for a 1 VDC drop in potential across the bus bars.

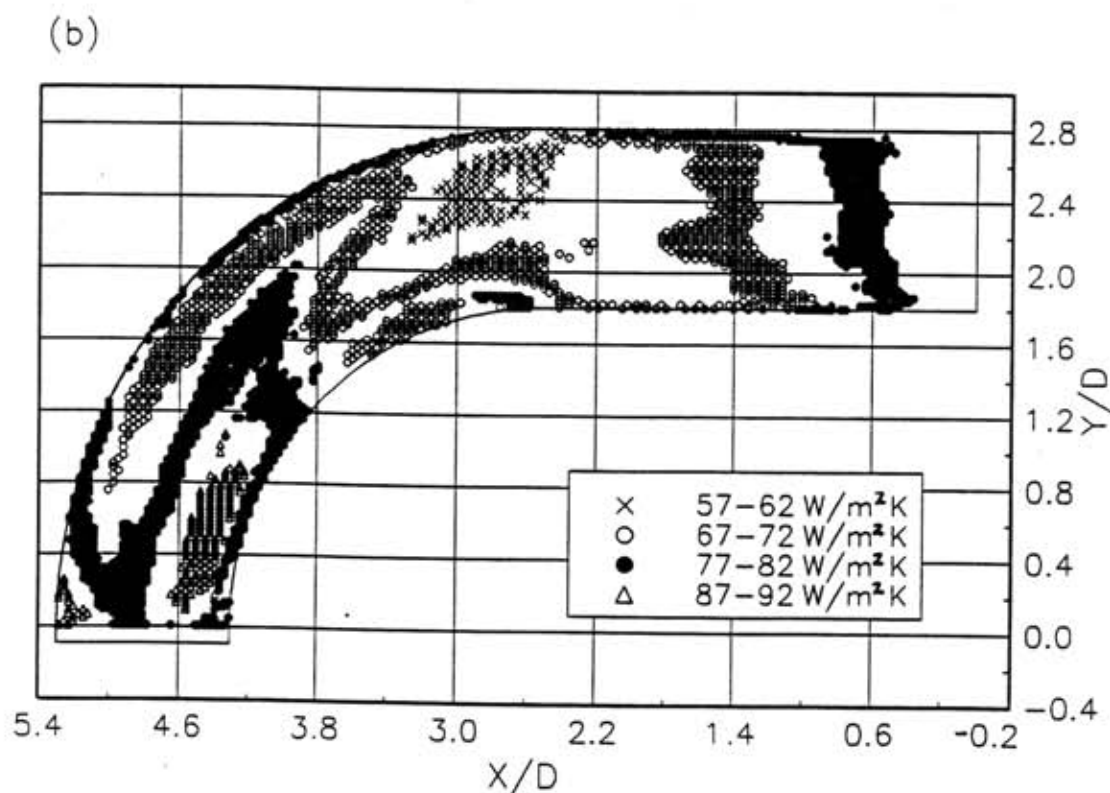
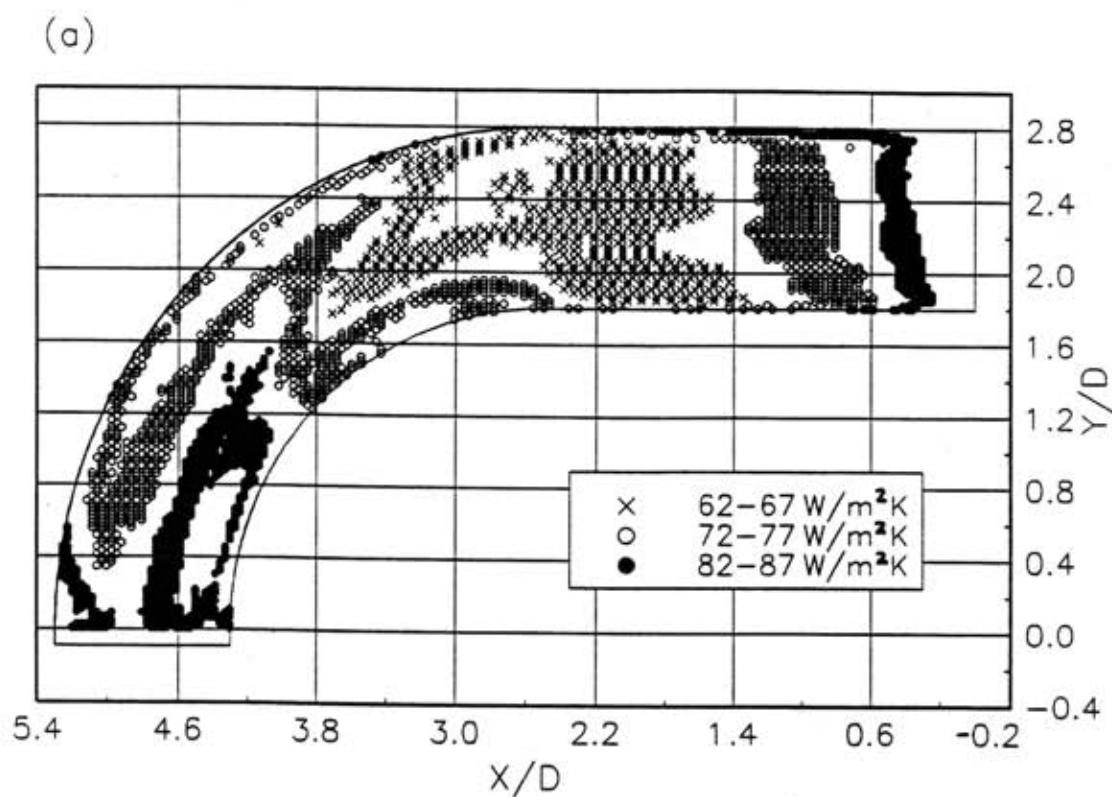


Fig. 5.11 (a) (b) Convective heat transfer coefficient ($\text{W/m}^2\text{K}$) distribution on the endwall surface. Data represents the results of twenty three processed images.

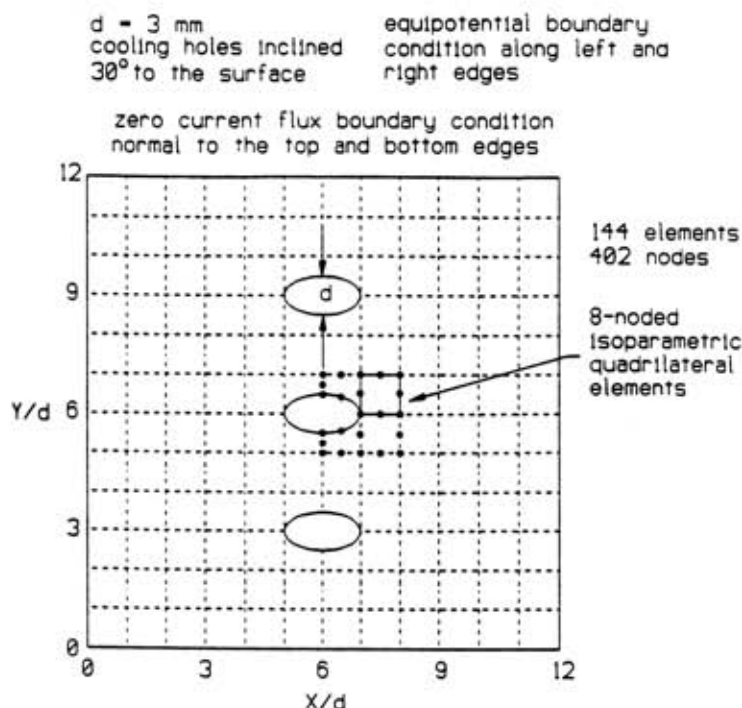


Fig. 5.12 Illustration of the heat flux surface geometry and finite element computational grid for a square surface with a 1×3 array of film cooling holes inclined 30° from the surface at a spacing of $Y/d=3$.

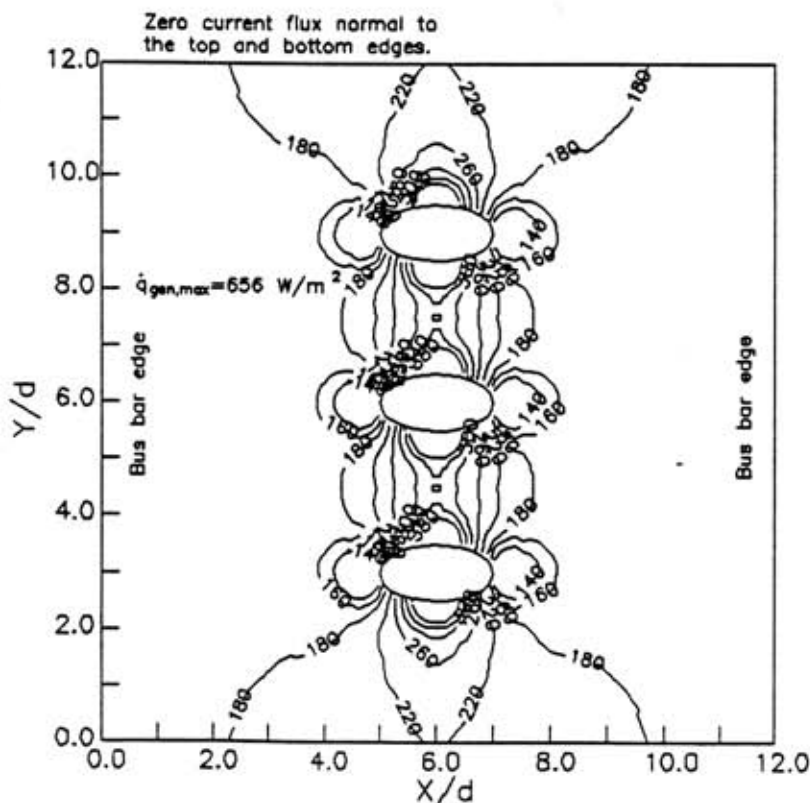


Fig. 5.13 Distribution of the generated heat flux (W/m^2) for a square surface that contains a 1×3 array of film cooling holes inclined 30° to the surface at a spacing of $Y/d=3$. Potential drop of 1 mVDC across the bus bars.